CO activation pathways and the mechanism of Fischer–Tropsch synthesis

Manuel Ojeda [a], Rahul Nabar [b], Anand U. Nilekar [b], Akio Ishikawa [a], Manos Mavrikakis [b,*], Enrique Iglesia [a,**]

[a] Department of Chemical Engineering, University of California at Berkeley, Berkeley, CA 94720, United States
[b] Department of Chemical and Biological Engineering, University of Wisconsin-Madison, Madison, WI 53706, United States

ARTICLE INFO

ABSTRACT

Unresolved mechanistic details of monomer formation in Fischer–Tropsch synthesis (FTS) and of its oxygen rejection routes are addressed here by combining kinetic and theoretical analyses of elementary steps on representative Fe and Co surfaces saturated with chemisorbed CO. These studies provide experimental and theoretical evidence for hydrogen-assisted CO activation as the predominant kinetically-relevant step on Fe and Co catalysts at conditions typical of FTS practice. H_2 and CO kinetic effects on FTS rates and oxygen rejection selectivity (as H_2O or CO_2) and density functional theory estimates of activation barriers and binding energies are consistent with H-assisted CO dissociation, but not with the previously accepted kinetic relevance of direct CO dissociation and chemisorbed carbon hydrogenation elementary steps. H-assisted CO dissociation removes O-atoms as H_2O, while direct dissociation forms chemisorbed oxygen atoms that desorb as CO_2. Direct CO dissociation routes are minor contributors to monomer formation on Fe and may become favored at high temperatures on alkali-promoted catalysts, but not on Co catalysts, which remove oxygen predominantly as H_2O because of the preponderance of H-assisted CO dissociation routes. The merging of experiment and theory led to the clarification of persistent mechanistic issues previously unresolved by separate experimental and theoretical inquiries.

© 2010 Elsevier Inc. All rights reserved.

1. Introduction

Fischer–Tropsch synthesis (FTS) converts synthesis gas (CO + H_2) into hydrocarbon chains; it is the preferred route for the production of chemicals and liquid fuels from natural gas, coal, and biomass [1–4]. Several mechanistic details remain unclear and speculative even after significant study. For instance, the specific CO dissociation pathways that form monomers and their kinetic consequences for chain growth remain largely unresolved. Fischer and Tropsch proposed a "carbide" mechanism, which involves direct CO dissociation and subsequent hydrogenation of chemisorbed carbon (C^*) to form CH_x monomers that initiate and grow hydrocarbon chains [5]. Storch and coworkers suggested that condensation of oxygen-containing intermediates (HCOH, hydroxycarbene) was responsible for C–C bond formation [6]. Several other proposals have since followed; they can be grouped into those involving direct dissociation of chemisorbed CO (CO^*) followed by reactions of its C^* and O^* products [7–13], and those in which chemisorbed hydrogen (H^*) adds to CO^* before C–O bond cleavage [13–16]. Only recently, theoretical investigations have probed the potential role of H-assisted CO dissociation in FTS on Fe and Co cat-

alysts [17–19] and in reactions involving C–O cleavage in the presence of H_2 [20,21], but without experimental verification.

Here, we provide experimental and theoretical evidence for the significant role of H-assisted pathways in kinetically-relevant CO dissociation steps on both Fe and Co catalysts at reaction conditions required for significant chain growth. Such pathways lead to the preferential rejection of the O-atoms in CO as H_2O via the direct formation of OH^* precursors through dissociation of the H_xCO species formed through interactions between chemisorbed hydrogen (H^*) and CO^*. These assisted pathways represent the exclusive CO activation routes on Co surfaces and the predominant one on Fe catalysts at relevant FTS conditions. H-assisted pathways occur concurrently with unassisted CO dissociation on Fe-based catalysts with oxygen rejection as CO_2. On Fe, the contributions from these two pathways are influenced by alkali promoters, often used to increase FTS rates and chain growth selectivities on Fe-based catalysts, which preferentially increase direct CO dissociation rates.

2. Methods

2.1. Catalyst preparation

Fe–Zn–Cu–K (Zn/Fe = 0.1, Cu/Fe = 0.03, and K/Fe = 0.06, atomic ratios) catalysts were prepared by co-precipitation of Fe and Zn oxides from 3 M Fe(NO$_3$)$_3$ (Sigma Aldrich, 98%) and 1.4 M Zn(NO$_3$)$_2$ (Sigma Aldrich, 98%) (Zn/Fe = 0.1) solutions [22]. The resulting

solution was added to 100 cm³ de-ionized water at 353 K and 120 cm³ h⁻¹ concurrently with a 1.0 M (NH₄)₂CO₃ (Sigma Aldrich, 99.9%) solution; the latter was added at a rate required to maintain a constant pH (7.0 ± 0.1). The precipitate (30 g) was rinsed with isopropanol (30 cm³ g⁻¹, Sigma Aldrich, 99.5%) five times to replace intrapellet water by a fluid with lower surface tension, which avoided loss of surface area during drying. Samples were treated in stagnant ambient air at 393 K for 12 h and then in flowing dry air (Praxair, UHP grade, 1.67 cm³ s⁻¹) by heating from ambient temperature to 543 K at 0.167 K s⁻¹ and holding for 4 h. Cu and K were sequentially added to Fe–Zn oxide precursors in this order via incipient wetness impregnation with aqueous solutions of Cu(NO₃)₂ (Aldrich, 99.99%) and K₂CO₃ (Aldrich, 99.99%), respectively. The solid was dried at 393 K for 12 h in ambient air after Cu addition. Following the K impregnation, the sample was dried in ambient air (393 K, 12 h) and treated again in flowing dry air (1.67 cm³ s⁻¹) by heating to 543 K at 0.167 K s⁻¹ and holding for 4 h.

2.2. Fischer–Tropsch synthesis rates and selectivities

FTS rates and selectivities were measured in a packed bed reactor with plug-flow hydrodynamics. Quartz granules (Sigma Aldrich, 11 g, 100–180 µm) were used as diluent for Fe–Zn–Cu–K catalysts (0.2 g, 100–180 µm) to prevent temperature gradients caused by exothermic FTS reactions. The diluents were treated at 298 K for 2 h in concentrated HNO₃ (Fisher, 69.5%, ACS reagent) and heated in ambient air at 973 K for 6 h to remove impurities. The catalyst was treated in flowing synthesis gas (Praxair, standard purity, H₂/CO = 2) at 101 kPa by heating from 298 K to 423 K at 0.167 K s⁻¹ and then from 423 to 543 K at 0.017 K s⁻¹ and holding for 1 h. The temperature was then decreased to 508 K and the H₂–CO pressure was increased gradually to the intended value. CO and H₂ pressures were varied in the range of 0.25–1.20 and 0.40–1.00 MPa, respectively, and a series of 3–4 space velocities were used at each condition. Concentrations in the inlet and effluent stream were measured on line by gas chromatography (HP 5890 Series II). A Porapak R packed column (Supelco, 2 m × 0.318 cm) with a thermal conductivity detector was used to analyze N₂, CO, CO₂, and CH₄, while C₁–C₁₅ olefins, paraffins, and oxygenates were analyzed using a flame-ionization detector and a cross-linked methyl silicone capillary column (HP–1, 50 m × 0.32 mm × 1.05 µm film). All transfer lines after the reactor were kept at 433–453 K to prevent condensation (except at a trap kept at 430 K to collect C₁₅₊ products) .

2.3. Theoretical analysis methods

All calculations were performed using DACAPO, a periodic self-consistent Density Functional Theory (DFT) based total-energy code [23,24], on the closest-packed facets of Fe and Co (Fe(1 1 0) and Co(0 0 0 1)). These model systems consisted of a four-layer slab, repeated periodically in a super-cell geometry with five equivalent layers of vacuum between any two successive metal slabs. A 2 × 2 surface unit cell was used, and the top two layers of the slab were allowed to relax. Adsorption occurred on only one of the two exposed surfaces of each slab, and the electrostatic potential was adjusted accordingly [25,26]. All adsorbed species were allowed to relax both during energy minimization and minimum energy path calculations. Ultrasoft pseudopotentials [27] were used to describe the ionic cores and a basis of plane waves with kinetic energy below 25 Ry expanded the Kohn–Sham one-electron valence states. Eighteen special Chadi–Cohen k-points were used to sample the surface Brillouin zone for Co(0 0 0 1), whereas a 16 k-point Monkhorst–Pack [28] grid was utilized for the Fe(1 1 0) surface. In all cases, convergence of the total energy with respect to calculation parameters, such as the k-point set,

number of included metal layers, and kinetic energy cut-off, was confirmed. The generalized gradient approximation (GGA-PW91) was used to describe the exchange–correlation energy and the potential self-consistently [29,30]. Iterative diagonalization of the Kohn–Sham Hamiltonian, the Fermi population of the Kohn–Sham states (k_BT = 0.1 eV), and the Pulay mixing of the resulting electronic density determined the self-consistent PW91 density [31]. Total energies were extrapolated to zero values of k_BT, and all calculations were performed spin-polarized for both Co and Fe systems. The calculated equilibrium PW91 lattice constants for bulk Fe and Co were found to be 2.85 and 2.51 Å, in excellent agreement with the experimental values of 2.87 and 2.51 Å, respectively [32,33].

The climbing-image nudged elastic band (CI-NEB) method [34–36] was used to determine minimum energy paths for all elementary steps described in this work. In each CI-NEB calculation, the minimum energy path between the initial and final state was discretized with at least seven intermediate images which were optimized iteratively. The image of highest energy along the reaction coordinate was designated as the transition state for each elementary step. The true nature of the saddle point was confirmed by vibrational frequency analysis yielding a single imaginary mode.

Diagonalization of the mass-weighted Hessian matrix, derived from a second-order finite-difference approximation (0.01 Å step size) of the PW91-calculated force derivatives, was used to determine vibrational frequencies [37]. Vibrational frequency calculations allowed the displacement of adsorbate atoms from their equilibrium positions while metal atoms remained fixed in their relaxed geometries. All other calculations, including structural optimization of adsorbed overlayers for all intermediates considered and for all CI-NEB calculations, were performed with complete relaxation of the top two metal layers in the slab and all adsorbed structures, including spectator CO molecules. To our knowledge, spectator CO molecules have not been previously included in electronic structure calculations for the specific surface chemistry addressed here. The additional computational cost seems appropriate because of the high CO coverages prevalent during FTS and the significant effects of spectator CO species on the binding energies of reactive intermediates and activation barriers of their elementary reactions.

3. Results and discussion

3.1. Influence of reactant pressures on hydrocarbon synthesis rates with Fe catalysts

Figs. 1 and 2 show CO conversion rates to hydrocarbons at 508 K on Fe–Zn–Cu–K as a function of CO conversion, which was varied by changing space velocity, at different inlet CO and H₂ pressures. Hydrocarbon synthesis rates decreased with increasing CO conversion in all cases, because of the combined effects of reactant depletion and inhibition by H₂O or CO₂ products. In what follows, rates have been extrapolated to zero CO conversion to avoid the kinetic complexities of reactant depletion and of inhibition by products.

Fig. 3 shows these extrapolated hydrocarbon synthesis rates as a function of CO and H₂ pressures. Hydrocarbon synthesis rates were proportional to H₂ pressure at all CO pressures. In contrast, rates were initially proportional to CO pressures below 0.36 MPa, but then approached constant values as pressure increased. The general trends observed with changes in H₂ and CO pressure are in qualitative agreement with those reported previously [12,38–41]. The dependence of hydrocarbon formation rates on H₂ and CO pressures was claimed to reflect the formation of C₁ monomers via direct CO dissociation to C* species that react with H* to form CHₓ* fragments [14]. As we show later, these proposals are inconsis-
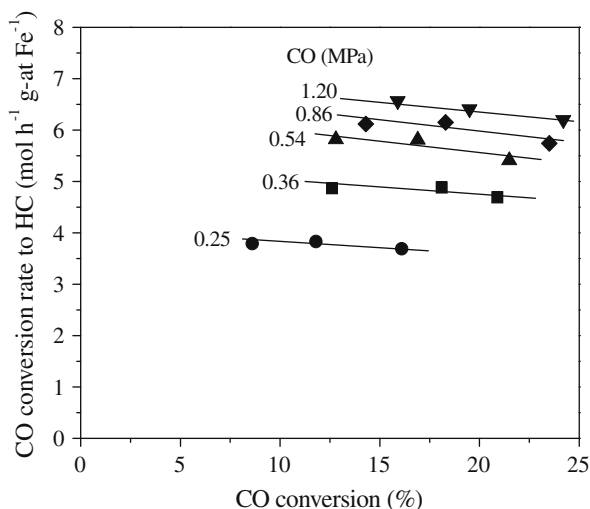
Fig. 1. Rate of CO conversion to hydrocarbons as a function of CO conversion at 0.25–1.20 MPa CO, 1.20 MPa H_2, and 508 K on Fe–Zn–Cu–K catalyst (●: 0.25; ■: 0.36; ▲: 0.54; ◆: 0.80; ▼: 1.20 MPa CO).
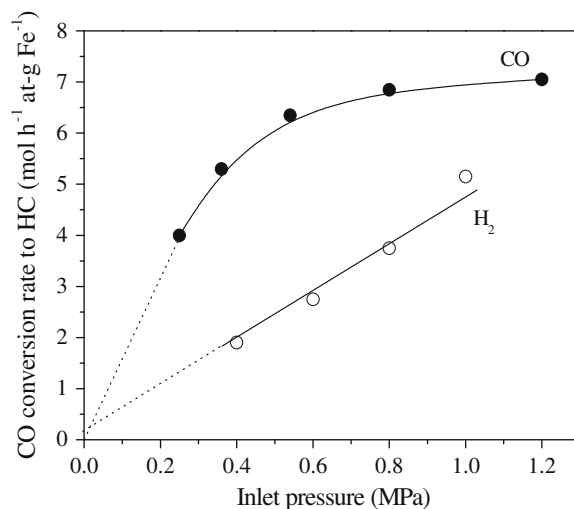

Fig. 3. Rate of CO conversion to hydrocarbons (extrapolated to zero CO conversion) at 0.25–1.20 MPa CO (●, 1.20 MPa H_2) and 0.40–1.00 MPa H_2 (○; 0.40 MPa CO) at 508 K on Fe–Zn–Cu–K catalyst.
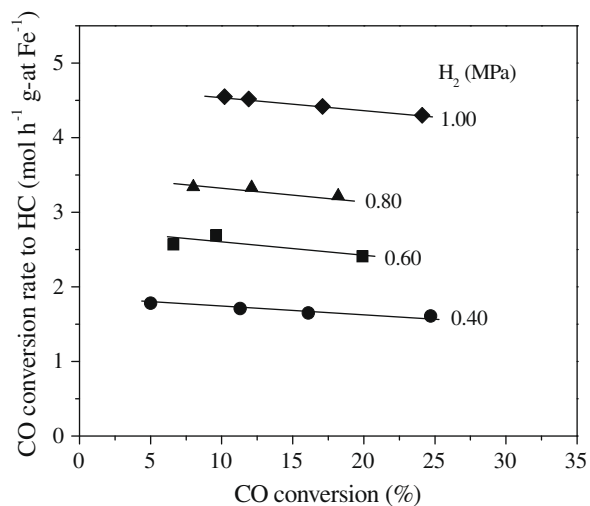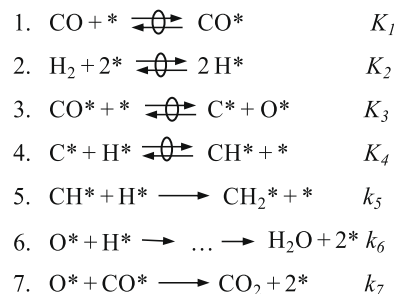

Fig. 2. Rate of CO conversion to hydrocarbons as a function of CO conversion at 0.40–1.00 MPa H_2, 0.40 MPa CO, and 508 K on Fe–Zn–Cu–K catalyst (●: 0.40; ■: 0.60; ▲: 0.80; ◆: 1.00 MPa H_2).

$$
\begin{array}{lll}
1. & CO + * \; \rightleftharpoons \; CO* & K_1 \\
2. & H_2 + 2* \; \rightleftharpoons \; 2\,H* & K_2 \\
3. & CO* + * \; \rightleftharpoons \; C* + O* & K_3 \\
4. & C* + H* \; \rightleftharpoons \; CH* + * & K_4 \\
5. & CH* + H* \; \longrightarrow \; CH_2* + * & k_5 \\
6. & O* + H* \; \longrightarrow \; \dots \; \longrightarrow \; H_2O + 2* & k_6 \\
7. & O* + CO* \; \longrightarrow \; CO_2 + 2* & k_7
\end{array}
$$

Scheme 1. Elementary steps for pathways involving unassisted CO dissociation and chemisorbed carbon intermediates.

$$
r = \frac{K_1 K_2 K_3 K_4 k_5 P_{CO} P_{H_2}}{(1 + K_1 P_{CO})^2} \tag{1}
$$

for the rate of formation of monomers, which also equals the rate of CO conversion to hydrocarbons (i.e. excluding CO converted to CO_2). This rate equation resembles some proposed previously without definitive mechanistic attribution on Fe and Co catalysts [40,42–47]. Some of the steps in Scheme 1, however, raise significant concerns because of the assumptions required in deriving Eq. (1) and because it provides, as we show next, an incomplete description of the rate data.

Eq. (1) requires *quasi*-equilibrated CO* dissociation via unassisted pathways, but DFT calculations show that CO dissociation barriers are 189 and 367 kJ mol^{-1} on CO-saturated Fe(1 1 0) and Co(0 0 0 1) surfaces, respectively (Tables 3 and 5). We discuss these calculations briefly here to highlight the concerns raised by the "carbide" mechanism; latter we provide details of the theoretical analysis in Sections 3.5 and 3.6. The calculated energy barriers for unassisted CO dissociation are much higher than previously reported activation energies on Fe and Co catalysts (80–120 kJ mol^{-1}) [12,48,49], suggesting that alternate routes for CO activation must be kinetically-accessible during FTS catalysis. Some recent studies have claimed alternate sites for CO dissociation, such as high index facets [50–52] or carbided surfaces [53], to overcome these inconsistencies. Such claims are, however, inconsistent with the higher turnover rates measured on larger Co clusters [55] and with the weaker binding of CO* on low-index surfaces, which would provide more abundant free sites required

tent with the activation barriers for CO dissociation and the addition of H* to C* as well as with the measured oxygen removal selectivities.

3.2. Mechanistic implications of measured rate equations for the formation of hydrocarbons and CO_2 over Fe and Co catalysts

The data described in the previous section led us to propose reaction schemes consistent with these findings and with the relative rates of O* rejection as H_2O and CO_2 and to probe their consistency with theoretical treatments of the elementary steps involved. Scheme 1 shows a sequence of elementary steps involving unassisted CO dissociation and subsequent H* addition to C* or O* to form CH_x* monomers and H_2O, as well as reactions of CO* with O* to form CO_2. CH_2* monomers then react in chain initiation and growth.

The *quasi*-equilibrium assumption for steps 1–4 with CO* and * as the most abundant reaction intermediates (MARI) for Scheme 1 gives:

for H* co-reactants and for CO dissociation than corner or edge sites prevalent on smaller clusters. Also, turnover rates decrease as Co clusters become smaller (<8 nm diameter) [54,55], consistent with preferential reactivity on low-index planes similar to those used in our simulations.

Several studies have proposed that active sites for FTS catalysis on Fe-based catalysts reside on Fe carbide surfaces [56,57]. We have also examined Fe(1 1 0) surfaces with near-surface carbide layers, formed via the facile diffusion of C-atoms formed in CO dissociation steps. The activation energy barrier for direct CO dissociation (CO* + * → C* + O*) on these surfaces (158 kJ mol^{-1}) remains higher than those measured on FTS catalysts. Recent studies have shown that H-assisted CO dissociation is more facile than direct CO dissociation on model Fe_5C_2(1 0 0) surfaces [58]. Other recent reports of the FTS reactivity of bulk Fe carbides do not provide clear evidence for the relative rates of CO dissociation on metal and carbide surfaces of Fe [53,59]. These difficulties reflect the diversity of possible structural models for Fe carbide surfaces and the markedly different reactivity of exposed facets with similar surface energies [60]. Similar conclusions about the relative rates of H-assisted and unassisted CO dissociation routes on carbided and metallic Fe surfaces led us to examine here plausible FTS mechanism by theoretical analysis of elementary steps on Fe(1 1 0) and Co(0 0 0 1) surfaces.

Chemisorbed oxygen (O*) formed via unassisted CO* dissociation can react via steps 6 or 7 (Scheme 1). Both steps involve similar activation barriers on Fe(1 1 0) (70 and 61 kJ mol^{-1}, for steps 6 and 7, respectively; Table 3). In contrast, the energy barrier for O* rejection as CO_2 on Co(0 0 0 1) surfaces (132 kJ mol^{-1}; Table 5) is significantly higher than for water formation (62 kJ mol^{-1}; Table 5). This suggests that oxygen removal as H_2O and CO_2 may occur concurrently on Fe catalysts, whereas Co would form only H_2O as the oxygen rejection product.

The energy barriers for the two forward and reverse sequential H* additions to O* indicate that water formation steps are irreversible on Fe(1 1 0) and Co(0 0 0 1) surfaces. Energy barriers for H* + O* → OH* + * and H* + OH* → H_2O + 2* on Fe(1 1 0) are 60 and 70 kJ mol^{-1}, respectively, while the reverse steps have respective barriers of 120 and 161 kJ mol^{-1}. On Co(0 0 0 1), the energy barriers are 47 and 62 kJ mol^{-1} for the forward H* addition steps and 151 and 205 kJ mol^{-1} for the respective reverse steps. The total O* removal rate to form H_2O and CO_2 then becomes:

$$r_{H_2O} = k_6 \cdot \theta_{H^*} \theta_{O^*} \quad (2)$$
$$r_{CO_2} = k_7 \cdot \theta_{CO^*} \theta_{O^*} \quad (3)$$

and the (H_2O/CO_2) ratios are given by (see Supplementary information for details):

$$\frac{r_{H_2O}}{r_{CO_2}} = \frac{K_2^{1/2} k_6}{K_1 k_7} \cdot \frac{P_{H_2}^{1/2}}{P_{CO}} \quad (4)$$

This direct CO dissociation sequence predicts that (H_2O/CO_2) ratios would increase with increasing (H_2/CO) ratio. Our data (Section 3.4) show instead that this ratio is independent of CO pressure and proportional to H_2 pressure, in contradiction with the predictions from unassisted CO dissociation pathways.

An additional concern is raised by the assumption that hydrogenation of C* (step 4) must be *quasi*-equilibrated, whereas the chemically similar step that subsequently hydrogenates CH* (step 5) is irreversible; these assumptions are essential for a kinetic equation consistent with the rate data, because the first-order kinetic dependence on H_2 pressure (Fig. 3) requires that step 5 be the sole kinetically-relevant step (Eq. (1)). In contrast with this, our theoretical treatment indicates that the addition of the first H* to C* on Fe(1 1 0) actually shows a higher activation barrier (74 kJ mol^{-1}) than the subsequent hydrogenation of CH*

(35 kJ mol^{-1}) and that neither step is likely to limit rates because of much higher barriers for the unassisted CO dissociation steps that precede steps 4 and 5 in Scheme 1. These calculations also show that the *equilibrium* surface coverage of CH* species would be higher than for C* ($\theta_{CH^*} > \theta_{C^*}$) at typical FTS conditions (see Supplementary information for details) and that CH* would be rapidly scavenged by subsequent H-addition steps, making C* reactions with H* the sole kinetically-relevant step. In this case, FTS rates would be proportional to $(H_2)^{0.5}$, in contradiction with rate data (Fig. 3). On Co(0 0 0 1) surfaces, both C* and CH* hydrogenation steps exhibit low and similar barriers (40 and 36 kJ mol^{-1} for steps 4 and 5, respectively), casting doubts on the kinetic relevance of either step, which is required for positive H_2 kinetic orders in FTS rates [40,41,55]. On Co, both steps 4 and 5 have much smaller activation barriers than for unassisted CO dissociation, making the assumption that step 5 (instead of CO dissociation) is the sole kinetically-relevant step inconsistent with these theoretical treatments. These inconsistencies between the activation energy barriers derived from theory and the assumptions required to describe measured rate data and O* removal selectivities led us to consider alternate catalytic sequences to resolve these previously unrecognized issues.

Recent studies have brought attention to the relevance of H-assisted CO dissociation routes on Fe, Co, and other transition metals [17–20,51,61,62]. Here, we bring additional rigor to these concepts by providing experimental confirmation and by demonstrating the need for spectator CO coverages for accurate FTS theoretical treatments. We consider in our analysis all plausible isomers of singly and doubly hydrogenated CO-derived intermediates [18,20] and show that second H-addition to these intermediates controls monomer formation rates. The resulting analysis is then used to compare Fe and Co surfaces and to provide a rigorous assessment of H-assisted CO dissociation routes. First, we examine CO_2 formation rates to provide additional evidence for the pre-eminent role of H-assisted pathways on both Fe and Co catalysts.

3.3. Primary and secondary CO_2 formation pathways on Fe catalysts

Fig. 4 shows that CO_2 formation rates (corrected for the approach to water–gas shift equilibrium; Supplementary information) on Fe–Zn–Cu–K increased with increasing CO conversion, which was varied by changing inlet CO molar rates, and with CO inlet pressures (1.2 MPa H_2; 508 K). These trends reflect the re-adsorption of H_2O formed as one of the primary O* removal products to re-form O*, which then reacts with CO* to form CO_2 in secondary reactions. These pathways contribute to exchange of O-atoms between CO_2 and H_2O, a reaction that reflects the water–gas shift stoichiometry, but which is rigorously described by elementary steps involved in FTS reactions.

CO_2 formation rates extrapolated to zero conversion reflect primary reactions of CO* with O* (Scheme 1, step 7), without contributions from re-adsorption and oxygen exchange. Primary CO_2 formation rates increased initially as CO pressure increased and then reached nearly constant values above 1.3 MPa CO; these rates were essentially independent of H_2 pressure (Fig. 5). These rate data are inconsistent with the kinetic expression derived from Scheme 1 for the rate of primary CO_2 formation (see Supplementary information for details):

$$r_{CO_2} = \frac{K_1^2 K_2 K_3 K_4 k_5 k_7 P_{CO}^2 P_{H_2}}{(K_2^{1/2} k_6 P_{H_2}^{1/2} + K_1 k_7 P_{CO})(1 + K_1 P_{CO})^2} \quad (5)$$

which would require significant effects of H_2 pressure, irrespective of the relative magnitudes of the various denominator terms. Measured rate data indicate that H_2-derived species are not involved in elementary steps leading to the formation of O*. These data indicate
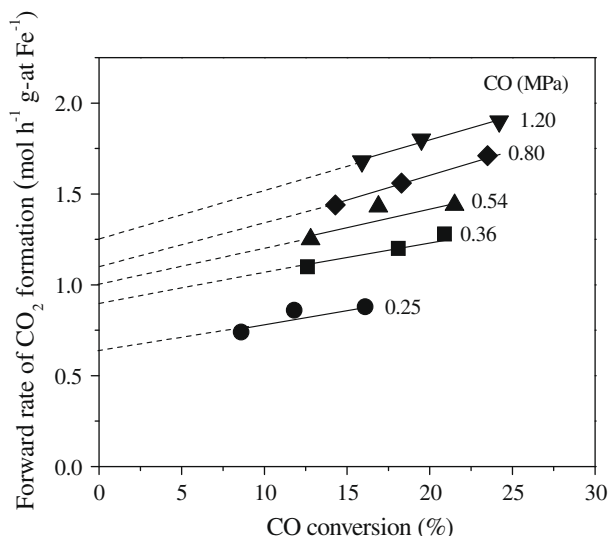
Fig. 4. Forward rate of CO_2 formation as a function of CO conversion at 0.25–1.20 MPa CO, 1.20 MPa H_2, and 508 K on Fe–Zn–Cu–K catalyst (●: 0.25; ■: 0.36; ▲: 0.54; ◆: 0.80; ▼: 1.20 MPa CO). See Supplementary information for details on forward rate calculation.
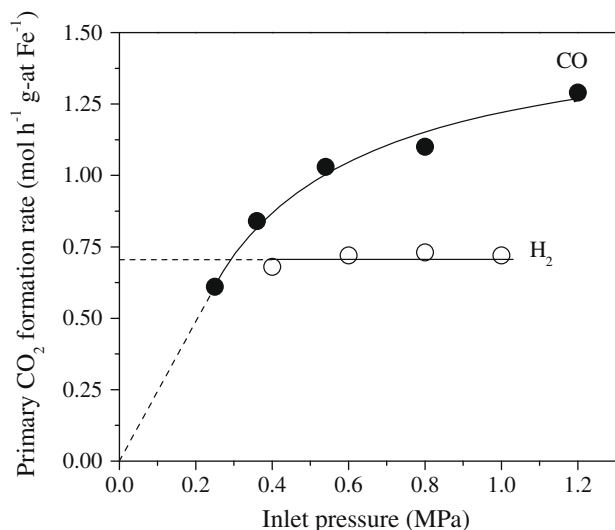

Fig. 5. Rate of CO_2 formation via primary routes at 0.25–1.20 MPa CO (●; 1.20 MPa H_2, 508 K) and 0.40–1.00 MPa H_2 (○; 0.40 MPa CO, 508 K) with Fe–Zn–Cu–K catalyst.
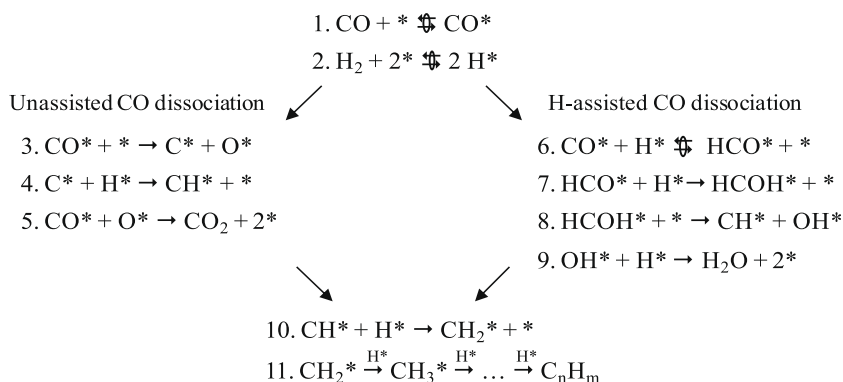
instead that primary CO_2 formation pathways involve only reactions of CO-derived intermediates formed without H_2 involvement, such as the unassisted dissociation of CO* and the subsequent removal of O* by CO*, in a sequence with the Boudouard reaction stoichiometry ($CO^* + CO^* \rightarrow C^* + CO_2^*$). We discuss next how a combination of H-assisted and unassisted CO dissociation steps leads to the parallel formation of H_2O and CO_2 as the molecular carriers of the O-atoms rejected during hydrocarbon synthesis.

3.4. Elementary steps involved in the Fischer–Tropsch synthesis on Fe catalysts

The measured effects of H_2 and CO pressures on hydrocarbon formation rate and H_2O/CO_2 product ratios on Fe–Zn–Cu–K led us to propose the sequence of elementary steps in Scheme 2, in which CO dissociates via parallel H-assisted and unassisted routes.

The unassisted route (step 3) forms C* and O* from CO*, while subsequent reactions with H* yield the CH_2^* monomers (steps 4, 10). The O* atoms formed in step 3 are removed as CO_2 via reactions with CO* (step 5). O* species could also react stepwise with H* to form H_2O. Indeed, our calculations show that on Fe(1 1 0), O* reactions with H* and CO* have similar activation barriers (60 and 61 kJ mol^{-1}, respectively; Table 3), but the predominant coverage by CO* (instead of H*) during steady-state catalysis, however, causes the preferential removal of any O* as CO_2 via reactions with CO*.

In the parallel H-assisted CO activation route (step 6, Scheme 2), CO* forms formyl intermediates (HCO*) via reactions with H*. On Fe(1 1 0), the activation barrier for H* addition to the C-atom in CO* (to form HCO*) is much smaller than for unassisted CO* dissociation (89 vs. 189 kJ mol^{-1}, respectively; Table 3). Subsequent hydrogenation at the O-atom in HCO* species forms hydroxymethylene (HCOH) intermediates. HCOH* dissociation then leads to CH* species that ultimately form monomers and initiators required for chain growth (step 10). OH* groups formed in step 8 are removed as H_2O in step 9. Alternatively, OH* may react with CO* to form carboxyl (COOH*) species, which would decompose subsequently to give CO_2 and H*. This latter step, however, would cause a kinetic effect of H_2 on primary CO_2 formation rates, which is not observed (Fig. 5). DFT calculations show that carboxyl formation has a higher activation energy barrier than water formation ($OH^* + H^* \rightarrow H_2O + 2^*$) by 24 kJ mol^{-1} on Fe(1 1 0). These activation barriers indicate that step 9 is the predominant mechanism for OH* removal, although the high (CO*)/(H*) ratios prevalent during FTS may offset, at least in part, these differences in activation barriers and cause detectable contributions from the carboxyl route in some cases. Subsequent COOH* decomposition steps, however, involve much higher barriers than those for step 9, on Pt and Cu surfaces [63,64], suggesting that carboxyl routes are unlikely to

1. $CO + ^* \rightleftharpoons CO^*$

2. $H_2 + 2^* \rightleftharpoons 2\,H^*$

Unassisted CO dissociation   H-assisted CO dissociation

3. $CO^* + ^* \rightarrow C^* + O^*$ 6. $CO^* + H^* \rightleftharpoons HCO^* + ^*$

4. $C^* + H^* \rightarrow CH^* + ^*$ 7. $HCO^* + H^* \rightarrow HCOH^* + ^*$

5. $CO^* + O^* \rightarrow CO_2 + 2^*$ 8. $HCOH^* + ^* \rightarrow CH^* + OH^*$

                                9. $OH^* + H^* \rightarrow H_2O + 2^*$

10. $CH^* + H^* \rightarrow CH_2^* + ^*$

11. $CH_2^* \overset{H^*}{\rightarrow} CH_3^* \overset{H^*}{\rightarrow} \ldots \overset{H^*}{\rightarrow} C_nH_m$

Scheme 2. Proposed elementary steps for FTS on Fe catalysts.

contribute to CO_2 formation during FTS. $COOH^*$ reactions with OH^* have lower barriers, but these bimolecular reactions are unlikely to occur on surfaces saturated with CO^*.

Next, we examine the kinetic consequences of the steps in Scheme 2 and show that these pathways accurately describe both hydrocarbon and CO_2/H_2O formation rates as a function of CO and H_2 pressures. Detailed theoretical calculations and their comparison with the assumptions, steps, and rate equations for the pathways in Scheme 2 are discussed in Section 3.5 and used to shed light on the chemical identity and structure of the various intermediates involved.

The parallel CO activation steps in Scheme 2 lead to additive contributions to hydrocarbon synthesis rates. These rates are given by:

$$r_{HC} = \frac{K_1 K_2 K_6 k_7 P_{H_2} P_{CO}}{(1 + K_1 P_{CO})^2} + \frac{K_1 k_3 P_{CO}}{(1 + K_1 P_{CO})^2} \tag{6}$$

when steps 1, 2, and 6 are *quasi*-equilibrated, and CO^* and * are the MARI during steady-state catalysis. The first term in Eq. (6) arises from H-assisted CO dissociation routes, while the second term reflects contributions from direct CO dissociation routes. In Eq. (6), the second term depends only on the CO pressure, because H_2-derived species are not involved in the kinetically-relevant CO dissociation step in the unassisted route depicted in Scheme 2. This term resembles Eq. (1) in functional form but differs in the chemical significance of the rate constants, which reflect in the case of Eq. (1), the equilibrated nature of steps 1–4 in Scheme 1, and the kinetic relevance of the second H-addition to C^* species derived from unassisted CO dissociation.

The two terms in Eq. (6) account also for the respective rates of H_2O and CO_2 formation, because the steps in Scheme 2 lead to H_2O only via OH^* formed via H-assisted routes and to CO_2 only via O^* formed in direct CO^* dissociation routes. As a result, the ratio of the two terms in Eq. (6) gives the (H_2O/CO_2) ratio formed in FTS reactions:

$$\frac{r_{H_2O}}{r_{CO_2}} = \frac{K_2 K_6 k_7}{k_3} \cdot P_{H_2} \tag{7}$$

This dependence is identical to that shown by the data in Fig. 6, in which the product ratio is proportional to H_2 pressure and independent of CO pressure. Fig. 6 also shows that (H_2O/CO_2) ratios are greater than unity for H_2 pressures above ~ 0.2 MPa, indicating that

H-assisted dissociation routes prevail during FTS catalysis even on Fe catalysts at H_2 pressures relevant to industrial practice (>1 MPa).

Table 1 shows the rate equations and kinetic parameters for hydrocarbon formation and oxygen rejection pathways on Fe–Zn–Cu–K catalysts. The Levenberg–Marquardt method [65] was used to estimate rate parameters from measured rates. The lumped kinetic parameters ($K_1 K_2 K_6 k_7$ and $K_1 k_3$) obtained from independent measurements of hydrocarbon formation and primary CO_2 formation rates are the same within the accuracy of the rate data. The equilibrium constant for CO adsorption (K_1; 0.77 ± 0.14 MPa^{-1} at 508 K) estimated from these data is similar to that reported from FTS data on Fe–Cu–K–SiO$_2$ catalysts at 523 K (0.54 ± 0.33 MPa^{-1}) [14]. The data and predictions shown in Fig. 7 show excellent agreement between hydrocarbon formation rate data and the values inferred from the mechanism-based rate equations in Table 1.

We proceed next to present detailed theoretical calculations of the binding energy of intermediates and the activation barriers for the elementary steps in Scheme 2 with emphasis on the pathways for oxygen rejection and for the hydrogenation of relevant surface intermediates.

3.5. Theoretical analysis of minimum energy pathways for CO activation and subsequent steps on Fe(1 1 0) surfaces saturated with CO^*

A theoretical treatment of the elementary steps in Scheme 2 requires that we determine the stability and binding energy of these intermediates on Fe(1 1 0). We obtain binding energies (E) from the total energies of uncovered surfaces (E_{clean}), of surfaces with adsorbed species (E_{ads}), and of the respective molecules in the gas phase (E_{gas}):

Table 1
Rate expressions and parameters for the FTS kinetic model.

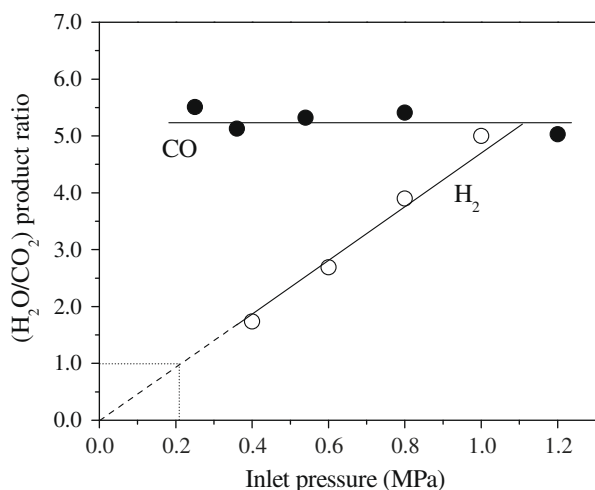| Rate expression	$K_1 K_2 K_6 k_7$ (mol h^{-1} g – at Fe^{-1} MPa^{-2})	$K_1 k_3$ (mol h^{-1} g – at Fe^{-1} MPa^{-1})
$r_{HC} = \frac{K_1 K_2 K_6 k_7 P_{CO} P_{H_2} + K_1 k_3 P_{CO}}{(1 + K_1 P_{CO})^2}$	16.0 ± 1.0	2.7 ± 0.4
$r_{H_2O} = \frac{K_1 K_2 K_6 k_7 P_{CO} P_{H_2}}{(1 + K_1 P_{CO})^2}$	15.7 ± 1.6	–
$r_{CO_2}^p = \frac{K_1 k_3 P_{CO}}{(1 + K_1 P_{CO})^2}$	–	3.5 ± 0.8

Fig. 6. Oxygen removal selectivity (H_2O/CO_2) at 0.25–1.20 MPa CO (●; 1.20 MPa H_2) and 0.40–1.00 MPa H_2 (○; 0.40 MPa CO) at 508 K on Fe–Zn–Cu–K catalyst.
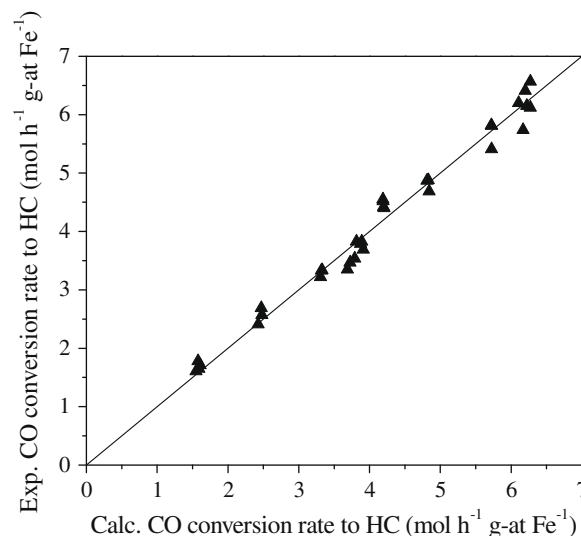

Fig. 7. Parity plot for the experimental and calculated CO conversion rate to hydrocarbons at 508 K on Fe–Zn–Cu–K catalyst.

$$E = E_{ads} - E_{clean} - E_{gas} \qquad (8)$$

More negative values reflect stronger interactions of adsorbed species with surface atoms. The binding of molecules (CO, CO_2, H_2, H_2O, CH_2O) and of relevant intermediates (C, O, H, CH, CH_2, OH, HCO, COH, HCOH) was examined at 0.25 MLcoverages on Fe(1 1 0) surfaces. Table 2 shows binding energies for the preferred binding sites of these species in their minimum-energy configurations. The calculated values agree with those reported previously [66–68].

CO^* binding energies on Fe(1 1 0) surfaces (-193 kJ mol^{-1}) are consistent with CO^* as the most abundant surface intermediate in kinetic treatments of FTS rate data [42]. These findings led us to examine chemisorbed species and their elementary reactions on CO^*-covered Fe(1 1 0) surfaces in all theoretical treatments that follow. First, we determined binding energies of CO^* as a function of CO^* coverage and specifically at 0.25, 0.5, 0.75, and 1.0 ML discrete coverages in (2×2) unit cells. CO binds more strongly at low coverages (-193 kJ mol^{-1} at 0.25 ML); both the average and the differential binding energies decreased with increasing CO^* coverage (Fig. 8). The differential adsorption energy for a CO molecule is given by:

$$E_{nCO}^{differential} = E_{slab+nCO} - E_{slab+(n-1)CO} - E_{CO_{gas}} \qquad (9)$$

where $E_{slab+nCO}$ and $E_{slab+(n-1)CO}$ are the total energies of the slab with n and $(n-1)$ adsorbed CO molecules, respectively, and $E_{CO_{gas}}$ is the total energy of CO in the gas phase. The differential CO chemisorption energy becomes zero between 0.75 and 1.0 ML, which defines the CO^* coverage at saturation. The CO^* binding weakens sharply at 0.75 ML, and as a result we use surfaces with 0.5 ML of fully-relaxed chemisorbed "spectator" CO^* species in all simulations described here. For instance, CO dissociation was probed by allowing one CO^* molecule in a surface covered with 0.75 ML CO^* to dissociate, leaving the surface with one C^*, one O^*, and 0.5 ML spectator CO^*.

Table 2 shows binding energies for various intermediates on Fe(1 1 0) surfaces with 0.5 ML spectator CO^*. All species (except H_2O) become more weakly-bound when co-adsorbed CO^* is present, with the strongest effects observed for HCO^* intermediates (binding energy weakens from -291 kJ mol^{-1} to -108 kJ mol^{-1}, when coverage of CO^* spectator increases from 0 to 0.5 ML; Table 2). This destabilization of adsorbed species reflects through-substrate and through-space repulsive interactions with CO^*. H_2O is the exception to these trends, because of H-bonding between H_2O^* and CO^*. The O–H distances between CO and H_2O molecules are consistent with H-bonding ($\sim$1.5 Å) [69]. On Fe(1 1 0), COH and

Table 2
Adsorption energies of various intermediates relevant in FTS with a clean and with 0.5 ML CO coverage on Fe(1 1 0) model surface.

Species	Adsorption energy (kJ mol^{-1})	
	Clean	0.5 ML CO*
C	−730	−657
O	−584	−473
CO	−193	−81
CO_2	−48	−15
H	−289	−246
H_2	−30	$\sim$0
CH	−660	−566
CH_2	−413	−296
OH	−366	−285
H_2O	−33	−69
HCO	−291	−108
COH	−455	−361
HCOH	−320	−193
CH_2O	−151	−36

Table 3
Energetics of the minimum energy paths for the FTS elementary steps on Fe(1 1 0) with 0.5 ML CO coverage. E_f, E_r, and ΔE refer to the forward barrier, reverse barrier, and heat of reaction, respectively, for each elementary step with respect to the species co-adsorbed on the surface.

Elementary step	Fe(1 1 0) with 0.5 ML CO coverage		
	E_f (kJ mol^{-1})	E_r (kJ mol^{-1})	ΔE (kJ mol^{-1})
$CO^* + ^* \rightarrow C^* + O^*$	189	164	25
$CO^* + H^* \rightarrow COH^* + ^*$	156	184	−28
$COH^* + H^* \rightarrow HCOH^* + ^*$	69	6	63
$HCOH^* + ^* \rightarrow CH^* + OH^*$	63	89	−26
$CO^* + H^* \rightarrow HCO^* + ^*$	89	12	77
$HCO^* + ^* \rightarrow CH^* + O^*$	76	70	6
$HCO^* + H^* \rightarrow HCOH^* + ^*$	68	101	−33
$HCO^* + H^* \rightarrow CH_2O^* + ^*$	58	168	−110
$CH_2O^* + ^* \rightarrow CH_2^* + O^*$	317	154	163
$COH^* + ^* \rightarrow C^* + OH^*$	157	101	56
$C^* + H^* \rightarrow CH^* + ^*$	74	104	−30
$CH^* + H^* \rightarrow CH_2^* + ^*$	35	32	3
$H_2 + 2^* \rightarrow H^* + H^*$	46	90	−44
$O^* + H^* \rightarrow OH^* + ^*$	60	120	−60
$OH^* + H^* \rightarrow H_2O + 2^*$	70	161	−91
$OH^* + OH^* \rightarrow H_2O^* + O^*$	53	114	−61
$CO^* + O^* \rightarrow CO_2 + 2^*$	61	256	−195

Table 4
Adsorption energies of various intermediates relevant in FTS with a clean and with 0.5 ML CO coverage on Co(0 0 0 1) model surface.

Species	Adsorption energy (kJ mol^{-1})	
	Clean	0.5 ML CO*
C	−647	−541
O	−524	−419
CO	−181	−75
CO_2	$\sim$0	$\sim$0
H	−278	−221
H_2	−35	$\sim$0
CH	−609	−529
CH_2	−372	−263
OH	−310	−255
H_2O	−28	−50
HCO	−216	−36
COH	−423	−360
HCOH	−289	−185
CH_2O	−85	−28

formaldehyde (CH_2O) are more stable than their respective isomers (HCO, formyl; HCOH, hydroxymethylene) (Table 2). Fig. 9 depicts the most stable structures for the intermediates in Scheme 2 on surfaces with 0.5 ML spectator CO^*.

Next, we address activation barriers for minimum energy pathways (MEP) of the elementary steps in Scheme 2 (Table 3). The preferred pathways for CO activation on a CO-saturated Fe(1 1 0) surface are shown in Fig. 10. In what follows, E_f, E_r and ΔE denote the forward barrier, the reverse barrier, and the energy of reaction (by convention, negative ΔE values imply exothermic steps) for each elementary step.

Direct CO^* dissociation is unfavorable compared with H-assisted dissociation, kinetically and thermodynamically, on CO-saturated Fe(1 1 0) surfaces ($\Delta E = 25$ kJ mol^{-1}, $E_f = 189$ kJ mol^{-1}). H-assisted pathways involve the initial addition of H^* to CO^* to form either formyls (HCO^*) or their COH^* isomers, which dissociate to give $CH^* + O^*$ or $C^* + OH^*$, respectively. The addition of a second H^* to HCO^* or COH^* before C–O cleavage may also occur; these latter steps form formaldehyde intermediates (CH_2O^*) or their hydroxymethylene ($HCOH^*$) isomers. C–O bond breaking in the latter species can then form $CH_2^* + O^*$ or $CH^* + OH^*$, respectively.

The relevance of these different pathways is examined next to probe preferred FTS routes on Fe surfaces. The results (Table 3;
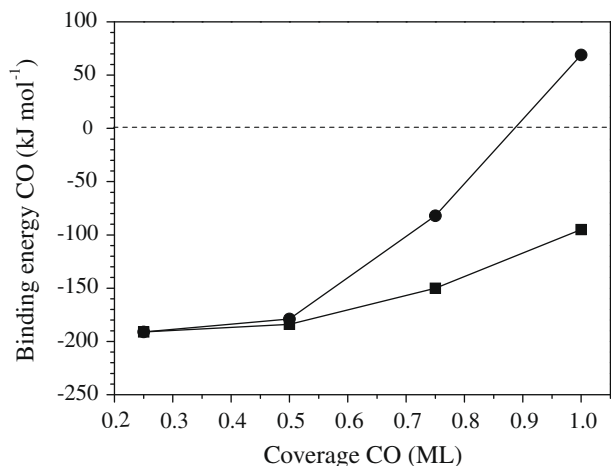
Fig. 8. Variation in CO adsorption energy (E_a) as a function of coverage on Fe(1 1 0) surfaces (■: average (or integral) energies; ●: differential energies). The dashed horizontal line at $E_a = 0$ kJ mol^{-1} highlights thermoneutral CO adsorption.
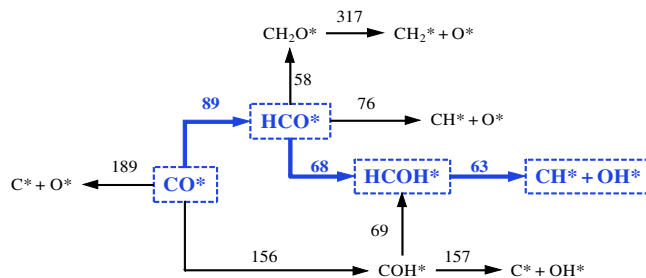

Fig. 10. Schematic of the FTS mechanism on Fe(1 1 0). Values on the arrows refer to the individual barriers (in kJ mol^{-1}) for each elementary step. The preferred H-assisted CO dissociation path is highlighted in blue. (For interpretation of the references to color in this figure legend, the reader is referred to the web version of this article.)

Fig. 10) indicate that H* addition to the C-atom in CO* to form HCO* ($E_f = 89$ kJ mol^{-1}) has a much lower barrier than addition to the O-atom to form COH* ($E_f = 156$ kJ mol^{-1}) or direct CO* dissociation ($E_f = 189$ kJ mol^{-1}). HCO* decomposition to H* and CO*, which reverses the first H-addition step in Scheme 2, occurs with a low barrier (12 kJ mol^{-1}), causing this step to become quasi-equilibrated during steady-state catalysis, consistent with experimental rate data. The preference for this route reflects the predominant CO* species prevalent during catalysis ((CO^*) $\gg$ (*)), which leads to kinetically-relevant concentrations of HCO* in spite of modestly unfavorable thermodynamics (77 kJ mol^{-1}) for this reaction ($CO^* + H^* \rightarrow HCO^* + ^*$). The addition of another H* to HCO* gives HCOH* with a low activation energy barrier ($E_f = 68$ kJ mol^{-1}), followed by facile dissociation to CH* and OH* ($E_f = 63$ kJ mol^{-1}). Alternatively, the addition of H* to the C-atom in HCO* gives CH$_2$O* with a 58 kJ mol^{-1} barrier; CH$_2$O* species can desorb as formaldehyde (CH$_2$O), which can then re-adsorb into pathways involved in monomer formation, or decompose to H$_2$ and CO in unproductive FTS pathways. The direct cleavage of the C–O bond in CH$_2$O* has a very high activation barrier ($E_f = 317$ kJ mol^{-1}), suggesting that it does not contribute to the formation of CH$_x$ monomers. CH$_2$O* species can form CH$_3$O* via hydrogenation with subsequent dissociation to form CH$_3^*$ + O*. The latter path does not form chain growth monomers and is therefore unproductive in hydrocarbon synthesis. C–O bond cleavage in HCO* species occurs with higher activation barriers than for H* addition to form HCOH* ($E_f = 76$ kJ mol^{-1} vs. 68 kJ mol^{-1}, respectively), consistent with the kinetic relevance of the second H-addition, instead of that of unimolecular HCO* decomposition.

So far, our treatment focused on the relative magnitude of activation barriers, but the relative coverage of the species involved in the various elementary steps also impacts their kinetic relevance, especially when activation barriers are similar among plausible elementary steps. For instance, the barriers for $CO^* + H^* \rightarrow HCO^*$

and $HCO^* + H^* \rightarrow HCOH^*$ on CO-saturated Fe surfaces are 89 kJ mol^{-1} and 68 kJ mol^{-1}, suggesting, at first glance, that the first H-addition may limit monomer formation rates. The difference in barriers for these two steps is 21 kJ mol^{-1}. If CO* coverages were 130 times larger than HCO* coverages, then the rates of these two steps would be similar (at 543 K). In fact, CO*/HCO* ratios are likely to be much larger than these values during steady-state FTS catalysis. Our theoretical estimates for binding energies and entropies, together with the assumption of equilibrated CO and H$_2$ adsorption, lead to CO*/HCO* ratios of $\sim 10^6$ for typical CO and H$_2$ pressures in this study (0.40–1.00 MPa H$_2$; 0.25–1.20 MPa CO). Thus, we conclude that the second hydrogen addition to CO* is the kinetically-relevant step in agreement with the assumptions required to describe rate data by the mechanism in Scheme 2. Similar conclusions were reached by parallel simulations and arguments on Co(0 0 0 1) surfaces.

Next, we probe the relative activation barriers for unassisted and H-assisted CO dissociation steps. The unassisted CO dissociation barrier is 189 kJ mol^{-1}, while those for the most facile steps involved in H-assisted routes are 89, 68, and 63 kJ mol^{-1} (for steps 6–8 in Scheme 2) (see also Fig. 10). The relative coverages of the intermediates involved may influence which specific step along the H-assisted route is kinetically-relevant, but in all cases unassisted CO dissociation steps are unlikely to contribute significantly to monomer formation and H-assisted routes prevail at all practical conditions, as also concluded from experiment.

Our proposed pathways (Scheme 2, Fig. 10) assume that the H* species required for reaction with CO*, HCO*, COH*, and other species form via *quasi*-equilibrated H$_2$ dissociation, consistent with the low H$_2$ dissociation barriers found on CO-saturated surfaces (~ 46 kJ mol^{-1}) and with previous experimental data on Co-based catalysts [70]. Alternate H$_2$ dissociation via direct reactions of H$_2$(g) or H$_2^*$ with CO* (to form COH* or HCO*) gave very high activation barriers (~ 192 kJ mol^{-1}), suggesting that these steps do not contribute to hydrogenation or CO activation pathways.

The thermodynamics (binding energies) and kinetics (activation barriers) of the intermediates in Scheme 2 lead us to conclude, in agreement with experiments, that H-assisted CO dissociation paths:
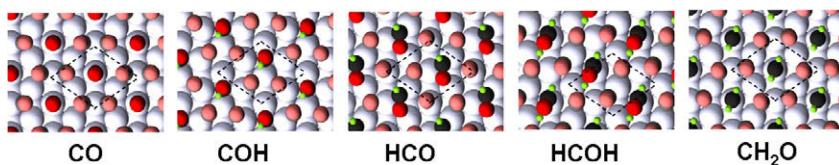

Fig. 9. Geometries and site preferences for FTS-relevant intermediates adsorbed on Fe(1 1 0) at 0.5 ML CO coverage. A representative 2 × 2 surface unit cell is delineated by dashed lines only as a guide to the eye, and the spectator CO molecules are colored a lighter color. Color map for atoms: black – carbon; red – oxygen; green – hydrogen; gray – iron. (For interpretation of the references to color in this figure legend, the reader is referred to the web version of this article.)

$$CO^* \rightarrow HCO^* \rightarrow HCOH^* \rightarrow CH^* + OH^* \qquad (10)$$
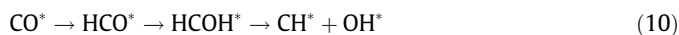
prevail on CO^*-covered surfaces during FTS catalysis. As shown from the effects of H_2 and CO on oxygen removal ratios (H_2O/CO_2), we find that H-assisted pathways form OH^* instead of O^* and that the latter (O^*) form CO_2 while the former (OH^*) is removed as H_2O. CH^* species resulting from the sequential hydrogenation steps Eq. (10) can be hydrogenated further to CH_2^* or CH_3^*, which act as monomers and initiators in the growth of hydrocarbon chains.

The calculated activation barriers for CH^* (from C^*) and CH_2^* (from CH^*) formation on CO-saturated Fe(1 1 0) indicate that the latter is the more facile step (Table 3). These conclusions are in sharp contrast with those reached in attempts to reconcile measured rates with those derived from elementary steps that dissociate CO^* exclusively via direct pathways [7,9–12], as we have discussed earlier.

Fig. 11 shows structural details of the initial, transition, and final states for each elementary step along the H-assisted CO activation path. $HCOH^*$ species have been proposed as reactive FTS intermediates [71], but the details of these steps are very different from those we report here. Several studies have proposed that alkanols can initiate chains during FTS on Fe catalysts [16,72], and complexes resembling $HCOH^*$ have been detected by their infrared spectra on such Fe catalysts [73], consistent with the presence of O-containing intermediates. The presence of $HCOH^*$ species provides plausible condensation routes to C_2 species that may be relevant in hydrocarbon formation, but such chain growth mechanistic details lie outside the scope of the present study.

Fe-based FTS catalysts tend to give larger CO_2/H_2O ratios than Co-based catalysts [70,74], suggesting that CO activation occurs exclusively via H-assisted routes on Co metal surfaces. In the next section, we probe the relative importance of the various elementary steps in Scheme 2 from estimates of the thermodynamics and activation barriers of the various adsorbed species in Scheme 2 for the case of Co(0 0 0 1) surfaces.

3.6. CO activation pathways and subsequent elementary steps on Co(0 0 0 1) surfaces saturated with CO^*

Minimum energy paths were examined on Co(0 0 0 1) surfaces saturated with CO^*. These low-index surfaces and saturation CO^* coverages are faithful representations of Co catalysts during FTS reactions, as shown by the measured rate equation and by the higher rates observed on larger Co clusters and their insensitivity to size for >8-nm clusters [54,55]. Coordinative unsaturation at edge or corner sites appears to be ineffective in FTS catalysis, in spite of their greater reactivity for CO^* dissociation, because of the unreactive nature of the C^* and O^* intermediates formed on such sites.

Binding energies for intermediates adsorbed on Co(0 0 0 1) are shown in Table 4. The binding energy of CO^* on Co(0 0 0 1) at 0.25 ML coverage (-181 kJ mol^{-1}) is consistent with CO^* as the most abundant surface intermediate during FTS catalysis, as also found on Fe(1 1 0). The binding and reactivity of adsorbed species in the presence of 0.5 ML CO^* are reported in Tables 4 and 5, respectively, for Co(0 0 0 1) surfaces. Direct CO^* dissociation on CO-saturated Co(0 0 0 1) surfaces proceeds with experimentally inaccessible activation barriers (367 kJ mol^{-1}), indicating that alternate routes are required for CO activation in FTS reactions. The highest barrier along the H-assisted CO^* activation route on Co(0 0 0 1) is only between 125 and 138 kJ mol^{-1}. Fig. 12 shows the minimum energy path for H-assisted CO dissociation steps on Co(0 0 0 1); the most likely preferred route is outlined in Eq. (10).

On Fe, the preference for H-addition at the C-atom (to form HCO^*) over the alternate path (addition at the O-atom to form COH^*) was evident from estimated barriers and from rate data that showed that the first H-addition step was equilibrated during FTS. The similar barriers for these two alternate paths on Co surfaces makes analogous conclusions less definitive based on these barriers alone, at least without a detailed microkinetic model and more detailed simulations on small Co nanoclusters (instead of the extended surfaces used here) at higher CO^* coverages. As in the case of Fe catalysts, measured rates indicate that the first H-addition to CO^* is equilibrated and the second H-addition is the kinetically-relevant step on Co catalysts. The calculated endothermic reaction energy for H-addition at the C-atom ($CO^* + H^* \rightarrow HCO^* + ^*$; Table 5) and the very exothermic nature of the alternate path ($CO^* + H^* \rightarrow COH^* + ^*$) indicate that the former (but not the latter) is likely to be equilibrated; thus, we conclude that in spite of its slightly higher activation barrier in the forward direction (138 kJ mol^{-1} vs. 125 kJ mol^{-1}), H-addition at the C-atom in CO is the most plausible pathway, because the alternate path, with its
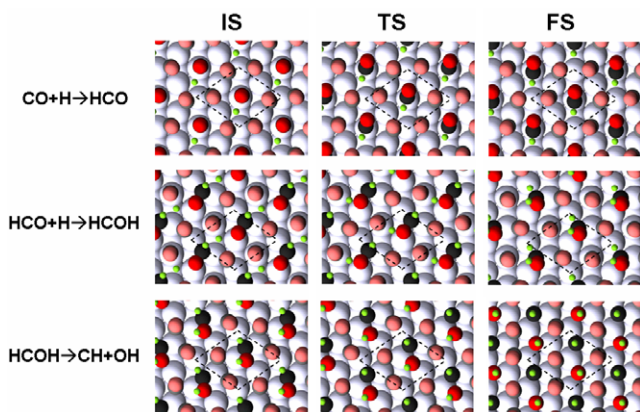

Fig. 11. Detailed structural information on the initial (IS), transition (TS), and final state (FS) involved in the minimum energy paths of the elementary steps for the H-assisted CO dissociation route on Fe(1 1 0) with 0.5 ML CO. A representative 2×2 surface unit cell is delineated by dashed lines only as a guide to the eye, and the spectator CO molecules are colored a lighter color. Color map for atoms: black – carbon; red – oxygen; green – hydrogen; gray – iron. (For interpretation of the references to color in this figure legend, the reader is referred to the web version of this article.)

Table 5
Energetics of the minimum energy paths for the FTS elementary steps on Co(0 0 0 1) with 0.5 ML CO coverage. E_f, E_r, and ΔE refer to the forward barrier, reverse barrier, and heat of reaction, respectively, for each elementary step with respect to the species co-adsorbed on the surface.

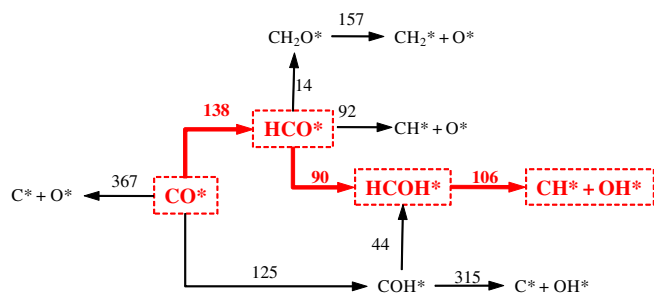| Elementary step	Co(0 0 0 1) with 0.5 ML CO coverage		
	E_f (kJ mol^{-1})	E_r (kJ mol^{-1})	ΔE (kJ mol^{-1})
$CO^* + ^* \rightarrow C^* + O^*$	367	115	252
$CO^* + H^* \rightarrow COH^* + ^*$	125	180	-55
$COH^* + H^* \rightarrow HCOH^* + ^*$	44	3	41
$HCOH^* + ^* \rightarrow CH^* + OH^*$	106	89	17
$CO^* + H^* \rightarrow HCO^* + ^*$	138	38	100
$HCO^* + ^* \rightarrow CH^* + O^*$	92	82	10
$HCO^* + H^* \rightarrow HCOH^* + ^*$	90	161	-71
$HCO^* + H^* \rightarrow CH_2O^* + ^*$	14	147	-133
$CH_2O^* + ^* \rightarrow CH_2^* + O^*$	157	78	79
$COH^* + ^* \rightarrow C^* + OH^*$	315	10	305
$C^* + H^* \rightarrow CH^* + ^*$	40	213	-173
$CH^* + H^* \rightarrow CH_2^* + ^*$	36	40	-4
$H_2 + 2^* \rightarrow H^* + H^*$	50	65	-15
$O^* + H^* \rightarrow OH^* + ^*$	47	151	-104
$OH^* + H^* \rightarrow H_2O + 2^*$	62	205	-143
$OH^* + OH^* \rightarrow H_2O^* + O^*$	29	152	-123
$CO^* + O^* \rightarrow CO_2 + 2^*$	132	261	-129

Fig. 12. Schematic of the FTS mechanism on Co(0 0 0 1). Values on the arrows refer to the individual barriers (in kJ mol^{-1}) for each elementary step. The preferred H-assisted CO dissociation path is highlighted in red. (For interpretation of the references to color in this figure legend, the reader is referred to the web version of this article.)

high barrier in the reverse direction (180 kJ mol^{-1} vs. 38 kJ mol^{-1} for the reverse of H* + CO* → HCO* + *), would not be equilibrated at typical FTS conditions. We cannot rule out, however, that both pathways could contribute to the formation of monomers during FTS reactions on small Co nanoclusters at CO* coverages higher than those probed in the present calculations on extended surfaces. We stress, however, that the actual position of the H-attack on CO* does not carry any implications for our conclusions and findings about the relevance of hydrogen assistance as the prevailing route for the activation of CO on Co surfaces.

On both Fe and Co, CH* and OH* then form via facile steps, leading to identical rate equations on these two surfaces. O* does not form on Co(0 0 0 1) because of the high activation barriers for unassisted CO dissociation. OH* species (formed via H-assisted routes) react with H* (instead of CO*) to form H$_2$O (instead of CO$_2$), consistent with the nearly exclusive removal of oxygen as H$_2$O on Co-based catalysts [70,74]. We conclude that primary CO$_2$/H$_2$O ratios during FTS provide an accurate diagnostic of the relative contributions of direct and H-assisted dissociation pathways. The direct CO dissociation barrier on Co is 229 kJ mol^{-1} higher than for H-assisted CO dissociation, while this difference is much smaller (100 kJ mol^{-1}) on Fe (Figs. 11 and 12), consistent with their respective tendencies to reject oxygen as CO$_2$.

The exclusive removal of oxygen as H$_2$O on Co-based catalysts is consistent with the prevalence of the H-assisted CO activation route and with the presence of a single term in the FTS rate equation on these catalysts:

$$r_{HC} = \frac{K_1 K_2 K_6 k_7 P_{H_2} P_{CO}}{(1 + K_1 P_{CO})^2} \tag{11}$$

Eq. (11) arises from the steps in the right side of Scheme 2 and equals the first term in the rate equation (Eq. (6)) found to describe FTS rates on Fe catalysts, which also reflects the contributions from H-assisted CO* dissociation pathways to monomer formation rates. Such Langmuir–Hinshelwood type equations accurately describe rate data on Co-based catalysts [40] and have been previously derived by assuming, without independent evidence, that formyl hydrogenation is the sole kinetically-relevant step on Co-based catalysts [47].

These H-assisted CO dissociation pathways remove conceptual hurdles in reconciling pathways mediated by direct CO dissociation with the lack of CO$_2$ in FTS products and with the first-order H$_2$ kinetic dependence on Co-based catalysts [46,55]. In such widely cited unassisted CO* activation mechanisms, the required assumption that hydrogenation of CH* species is the sole kinetically-relevant step is inconsistent with theoretical treatments (Table 5), which shows that H* addition to C* or CH* occurs with similar activation barriers (36–40 kJ mol^{-1}).

3.7. Unifying concepts in FTS catalysis on cobalt and iron catalysts

The theoretical and experimental evidence reported here resolves long-standing conflicts among measured rates, theoretical insights, and oxygen rejection selectivities on Co and Fe catalysts. H-atoms (formed via quasi-equilibrated H$_2$ dissociation) are ubiquitously involved in all elementary steps required for CO dissociation and for the formation of chain growth monomers. When direct dissociation pathways contribute significantly, as they do at higher temperatures, especially on alkali-promoted Fe catalysts, they form O* species that are ultimately rejected as CO$_2$. These conclusions are consistent with experimental and theoretical values of H$_2$/D$_2$ isotope effects reported previously [70] and which will be discussed in a separate study [75]. We find that the direct CO dissociation term in Eq. (6) shows no detectable H$_2$–D$_2$ isotope effects, while the first term in Eq. (6) exhibits the thermodynamic and kinetic isotopic effects expected from theoretical treatments of the elementary steps in Scheme 2.

We note that synergies among accurate rate data of demonstrated chemical kinetic origins, rigorous kinetic analysis of elementary step sequence, and theoretical treatments of representative densely covered Fe and Co surfaces can be used to probe and establish a sequence of elementary steps common to both types of catalysts. In doing so, this study resolves persistent conceptual hurdles and mechanistic inconsistencies. The results and analysis reported here provide compelling evidence for the critical role of the bimolecular intervention of chemisorbed hydrogen atoms in the activation of CO* on saturated surfaces. These conclusions seem reasonable in light of the dearth of vacant surface sites prevalent at reactant pressures required for significant chain growth in Fischer–Tropsch synthesis practice.

4. Conclusions

Experimental data and theoretical calculations evidence two parallel CO activation pathways on CO-covered Fe catalysts: unassisted and H-assisted. Both routes form CH$_2^*$ monomers, but they differ in oxygen rejection pathways. The unassisted CO activation removes O* as CO$_2$, while the H-assisted pathway forms H$_2$O exclusively. The kinetic expression derived by rigorous analysis of the resulting sequence of elementary steps is consistent with the measured dependence of FTS rates on H$_2$ and CO pressures. Oxygen removal selectivities indicate that H-assistance prevails on CO*-covered Fe surfaces. The minimum energy paths obtained from DFT calculations on realistic (CO covered) Fe model surfaces are in agreement with the FTS mechanism proposed here. These calculations also reveal the identity of the reaction intermediates involved in CO* activation pathways.

For Co catalysts, we have found by theoretical analysis that unassisted CO* activation is not competitive with the H-assisted route, leading to oxygen rejection pathways as H$_2$O exclusively, consistent with previous reports. Monomer formation via the H-assisted CO activation route would completely dominate on Co catalysts. The obtained rate expression for hydrocarbon synthesis is also consistent with experimental data reported in the literature.

Appendix A. Supplementary material

Supplementary data associated with this article can be found, in the online version, at doi:10.1016/j.jcat.2010.04.012.

References

[1] H. Schulz, Appl. Catal. A: Gen. 186 (1999) 3.
[2] M.E. Dry, Catal. Today 71 (2002) 227.
[3] M.J.A. Tijmensen, A.P.C. Faaij, C.N. Hamelinck, M.R.M. van Hardeveld, Biomass Bioenergy 23 (2002) 129.
[4] R.W.R. Zwart, H. Boerrigter, Energy Fuels 19 (2005) 591.
[5] F. Fischer, H. Tropsch, Brennst. Chem. 7 (1926) 97.
[6] H.H. Storch, N. Golumbic, R.B. Anderson, The Fischer–Tropsch and Related Syntheses, Wiley, New York, 1951.
[7] A.T. Bell, Catal. Rev. Sci. Eng. 23 (1981) 203.
[8] A. Erdohelyi, F. Solymosi, J. Catal. 84 (1983) 446.
[9] V. Ponec, Catal. Today 12 (1992) 227.
[10] M.E. Dry, Appl. Catal. A: Gen. 138 (1996) 319.
[11] A.A. Adesina, Appl. Catal. A: Gen. 138 (1996) 345.
[12] S.A. Eliason, C.H. Bartholomew, Appl. Catal. A: Gen. 186 (1999) 229.
[13] B.H. Davis, Catal. Today 141 (2009) 25.
[14] G.P. van der Laan, A.A.C.M. Beenackers, Appl. Catal. A: Gen. 193 (2000) 39.
[15] S. Storsæter, D. Chen, A. Holmen, Surf. Sci. 600 (2006) 2051.
[16] W.K. Hall, R.J. Kokes, P.H. Emmett, J. Am. Chem. Soc. 82 (1960) 1027.
[17] C.F. Huo, Y.W. Li, J. Wang, H. Jiao, J. Phys. Chem. C 112 (2008) 14108.
[18] C.F. Huo, J. Ren, Y.W. Li, J. Wang, H. Jiao, J. Catal. 249 (2007) 174.
[19] O.R. Inderwildi, S.J. Jenkins, D.A. King, J. Phys. Chem. C 112 (2008) 1305.
[20] M.P. Andersson, F. Abild-Pedersen, I.N. Remediakis, T. Bligaard, G. Jones, J. Engbaek, O. Lytken, S. Horch, J.H. Nielsen, J. Sehested, J.R. Rostrup-Nielsen, J.K. Nørskov, I. Chorkendorff, J. Catal. 255 (2008) 6.
[21] G.A. Morgan, D.C. Sorescu, T. Zubkov, J.T. Yates, J. Phys. Chem. B 108 (2004) 3614.
[22] S. Li, A. Li, S. Krishnamoorthy, E. Iglesia, Catal. Lett. 77 (2001) 197.
[23] B. Hammer, L.B. Hansen, J.K. Nørskov, Phys. Rev. B 59 (1999) 7413.
[24] J. Greeley, J.K. Nørskov, M. Mavrikakis, Annu. Rev. Phys. Chem. 53 (2002) 319.
[25] J. Neugebauer, M. Scheffer, Phys. Rev. B 46 (1992) 16017.
[26] L. Bengtsson, Phys. Rev. B 59 (1999) 12301.
[27] D. Vanderbilt, Phys. Rev. B 41 (1990) 7892.
[28] H.J. Monkhorst, J.D. Pack, Phys. Rev. B 13 (1976) 5188.
[29] J.P. Perdew, J.A. Chevary, S.H. Vosko, K.A. Jackson, M.R. Pederson, D.J. Singh, C. Fiolhais, Phys. Rev. B 46 (1992) 6671.
[30] J.A. White, D.M. Bird, Phys. Rev. B 50 (1994) 4954.
[31] G. Kresse, J. Furthmuller, Comput. Mater. Sci. 6 (1996) 15.
[32] P. Villers, L.D. Calvert, Pearson's Handbook of Crystallographic Data for Intermetallic Phases, ASTM International, Newbury, 1991.
[33] D.R. Lide, H.P.R. Frederikse, CRC Handbook of Chemistry and Physics, 1997.
[34] G. Henkelman, B.P. Uberuaga, H. Jonsson, J. Chem. Phys. 113 (2000) 9901.
[35] H.J. Jonsson, G. Mills, K.W. Jacobsen, Classical and Quantum Dynamics in Condensed Phase Simulations, Singapore, 1998.
[36] G. Henkelman, H. Jonsson, J. Chem. Phys. 113 (2000) 9978.
[37] J. Greeley, M. Mavrikakis, Surf. Sci. 540 (2003) 215.
[38] T.K. Das, W.A. Conner, J. Li, G. Jacobs, M.E. Dry, B.H. Davis, Energy Fuels 19 (2005) 1430.
[39] G.A. Huff, C.N. Satterfield, Ind. Eng. Chem. Proc. Des. Dev. 23 (1984) 696.
[40] I.C. Yates, C.N. Satterfield, Energy Fuels 5 (1991) 168.
[41] R. Zennaro, M. Tagliabue, C.H. Bartholomew, Catal. Today 58 (2000) 309.
[42] G.P. van der Laan, A.A.C.M. Beenackers, Catal. Rev. Sci. Eng. 41 (1999) 255.
[43] R.A. Dictor, A.T. Bell, J. Catal. 97 (1986) 121.
[44] K. Herzog, J. Gaube, J. Catal. 115 (1989) 337.
[45] F.G. Botes, Ind. Eng. Chem. Res. 48 (2009) 1859.
[46] A.O.I. Rautavuoma, H.S. Vanderbaan, Appl. Catal. 1 (1981) 247.
[47] B. Sarup, B.W. Wojciechowski, Can. J. Chem. Eng. 67 (1989) 62.
[48] H.P. Withers, K.F. Eliezer, J.W. Mitchell, Ind. Eng. Chem. Res. 29 (1990) 1807.
[49] W.D. Deckwer, Y. Serpemen, M. Ralek, B. Schimdt, Ind. Eng. Chem. Proc. Des. Dev. 21 (1982) 222.
[50] D. Borthwick, V. Fiorin, S.J. Jenkins, D.A. King, Surf. Sci. 602 (2008) 2325.
[51] S. Shetty, A.P.J. Jansen, R.A. van Santen, J. Am. Chem. Soc. 131 (2009) 12874.
[52] D.C. Sorescu, J. Phys. Chem. C 112 (2008) 10472.
[53] D.C. Sorescu, J. Phys. Chem. C 113 (2009) 9256.
[54] J.P. den Breejen, P.B. Radstake, G.L. Bezemer, J.H. Bitter, V. Froseth, A. Holmen, K.P. de Jong, J. Am. Chem. Soc. 131 (2009) 7197.
[55] E. Iglesia, S.C. Reyes, R.J. Madon, S.L. Soled, Adv. Catal. 39 (1993) 221.
[56] T. Herranz, S. Rojas, F.J. Pérez-Alonso, M. Ojeda, P. Terreros, J.L.G. Fierro, J. Catal. 243 (2006) 199.
[57] R.J. ÓBrien, L. Xu, R.L. Spicer, B.H. Davis, Energy Fuels 10 (1996) 921.
[58] J. Gracia, F. Prinsloo, J. Niemantsverdriet, Catal. Lett. 133 (2009) 257.
[59] M.A. Petersen, P.J. Steynberg, J.A. van der Ber, W.J. van Rensburg In: Abst. Papers 237th ACS National Meeting, Salt Lake City, Utah, 2009.
[60] P.J. Steynberg, J.A. van den Berg, W.J. van Rensburg, J. Phys.: Condens. Matter 20 (2008) 064238.
[61] J. Chen, P. Hu, P. Ellis, S. French, G. Kelly, C. Martin Lok, J. Phys. Chem. C 112 (2008) 9464.
[62] O.R. Inderwildi, S.J. Jenkins, D.A. King, Angew. Chem. Int. Ed. 47 (2008) 5253.
[63] L.C. Grabow, A.A. Gokhale, S. Evans, J.A. Dumesic, M. Mavrikakis, J. Phys. Chem. C 112 (2008) 4608.
[64] A.A. Gokhale, J.A. Dumesic, M. Mavrikakis, J. Am. Chem. Soc. 130 (2008) 1402.
[65] D.W. Marquardt, SIAM J. Appl. Math. 11 (1963) 431.
[66] D.C. Sorescu, Phys. Rev. B 73 (2006) 155420.
[67] Q. Ge, M. Neurock, H.A. Wright, N. Srinivasan, J. Phys. Chem. B 106 (2002) 2826.
[68] D.J. Klinke, D.J. Dooling, L.J. Broadbelt, Surf. Sci. 425 (1999) 334.
[69] P. Atkins, J. de Paula, Physical Chemistry, W.H. Freeman, New York, 2001.
[70] S. Krishnamoorthy, M. Tu, M.P. Ojeda, D. Pinna, E. Iglesia, J. Catal. 211 (2002) 422.
[71] R.B. Anderson, J.F. Schultz, Bull. United States Bureau Mines 580 (1959) 25.
[72] J.T. Kummer, P.H. Emmett, J. Am. Chem. Soc. 75 (1953) 5177.
[73] G. Blyholder, L.D. Neff, J. Phys. Chem. 66 (1962) 1664.
[74] M.J. Keyser, R.C. Everson, R.L. Espinoza, Ind. Eng. Chem. Res. 39 (2000) 48.
[75] M. Ojeda, A. Li, R. Nabar, A.U. Nilekar, M. Mavrikakis, E. Iglesia, in preparation.